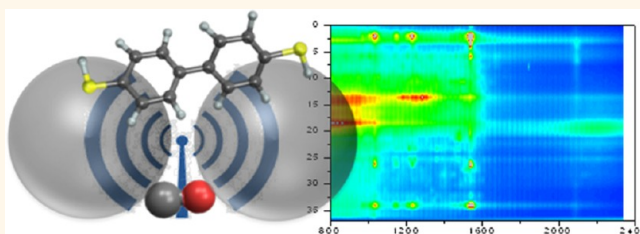# Surface-Enhanced Raman Trajectories on a Nano-Dumbbell: Transition from Field to Charge Transfer Plasmons as the Spheres Fuse

Mayukh Banik,[†] Patrick Z. El-Khoury,[†,§] Amit Nag,[†] Alejandro Rodriguez-Perez,[†] Nekane Guarrottxena,[‡] Guillermo C. Bazan,[‡] and Vartkess A. Apkarian[†,*]

[†]Department of Chemistry, University of California, Irvine, California 92697, United States and [‡]Department of Chemistry, University of California, Santa Barbara, California 93106, United States. [§]Present address: Pacific Northwest National Laboratory.

**ABSTRACT**  By taking advantage of the tensor nature of surface-enhanced Raman scattering (SERS), we track trajectories of the linker molecule and a CO molecule chemisorbed at the hot spot of a nano-dumbbell consisting of dibenzyldithio-linked silver nanospheres. The linear Stark shift of CO serves as an absolute gauge of the local field, while the polyatomic spectra characterize the vector components of the local field. We identify surface-enhanced Raman optical activity due to a transient asperity in the nanojunction in an otherwise uneventful SERS trajectory. During fusion of the spheres, we observe sequential evolution of the enhanced spectra from dipole-coupled Raman to quadrupole- and magnetic dipole-coupled Raman, followed by a transition from line spectra to band spectra, and the full reversal of the sequence. From the spectrum of CO, the sequence can be understood to track the evolution of the junction plasmon resonance from dipolar to quadrupolar to charge transfer as a function of intersphere separation, which evolves at a speed of ~1 Å/min. The crossover to the conduction limit is marked by the transition of line spectra to Stark-broadened and shifted band spectra. As the junction closes on CO, the local field reaches 1 V/Å, limited to a current of 1 electron per vibrational cycle passing through the molecule, with associated Raman enhancement factor *via* the charge transfer plasmon resonance of $10^{12}$. The local field identifies that a sharp protrusion is responsible for room-temperature chemisorption of CO on silver. The asymmetric phototunneling junction, Ag—CO—Ag, driven by the frequency-tunable charge transfer plasmon of the dumbbell antenna, combines the design elements of an ideal rectifying photocollector.

**KEYWORDS:** SERS · SEROA · plasmon · charge transfer plasmon · break junction · dumbbell · nanosphere · dibenzyldithiol · biphenyl · carbon monoxide · rectenna · antenna

Raman spectroscopy of single molecules is accessible at junctions of metallic nanostructures, where local fields are dramatically enhanced by the plasmonic response.[1] Since Raman scattering is a tensor quantity and local fields of nanojunctions are inhomogeneous on molecular length scales, given knowledge of the local field, spectra should be sufficient to track the location and orientation of molecules in 3D space. Alternatively, given knowledge of the molecular polarizability tensor, spectra should be sufficient to determine the local vector field. We implement this proposition through measurements on the prototypical junction formed between two metallic nanospheres.[2−5] A chemically engineered nano-dumbbell consisting of dibenzyldithio-linked silver spheres (~30 nm diameter) serves as our experimental platform, with all evidence indicating that we are tracking single molecules.[6,7] Two illustrative spectral sequences will be presented: An uneventful sequence, which highlights optical activity of the junction and the spectral sensitivity to orientation that can be attained. A more eventful trajectory is recorded during the fusion of the nanospheres. The sequence identifies line spectra due to surface-enhanced dipole−quadrupole Raman (SEQRS), surface-enhanced dipole−magnetic dipole Raman (SEMRS),[8] and band spectra when the junction gap reaches the conductivity limit of plasmons.[9−13] In good agreement

with recent quantum analysis,[12,13] as the junction gap closes, we see the progressive tuning of plasmon resonances from the bonding dipole plasmon (BDP) to the bonding quadrupole plasmon (BQP), to the charge transfer plasmon (CTP). The latter is most clearly illustrated through SERS of an unintentionally chemisorbed CO molecule at the hot spot. Our analysis clarifies continua (band spectra) that commonly appear in SERS arise from CTP resonances. The observations of magnetic and quadrupolar Raman spectra confirm surface-enhanced Raman optical activity (SEROA),[14] which although reported[15−17] has been contested on general grounds.[18] The process can be driven by multipolar fields, which arise when nanometric asperities decorate the junction. The single-molecule nature of the measurements allows such compelling mechanistic assignments of SERS.

In standard implementations of Raman spectroscopy on molecular ensembles, orientational averaging contracts the observables to intensities and depolarization ratios of vibrational modes.[19] Moreover, the appropriate long-wave limit ($\langle r \rangle/\lambda \sim 10^{-3}-10^{-4}$, where $r$ is the molecular length scale and $\lambda$ is the wavelength of light) implies that only the local response to field amplitudes determines scattering matrix elements. For single molecules immobilized on the time scale of detection, the full tensor nature of the scattering process comes to force. The intensity of a given vibrational mode is now dictated by the orientation of the molecule relative to the vector field. Moreover, since local fields at nanojunctions vary on nanometer scale, $\langle r \rangle/\lambda \sim 1$, the response is nonlocal.[20] Therefore, a multipolar expansion of the molecular response and local fields is necessary to interpret spectra. Where either the junction or molecule is not stationary, spectra fluctuate, as extensively catalogued ever since the earliest single-molecule SERS measurements.[21] We equate fluctuating spectra to single-molecule trajectories tracked through far-field measurements akin to global positioning with local antennae. The prerequisites for such tracking are (a) knowledge of local fields, which in the classical limit can be reliably obtained through finite element analysis, and (b) knowledge of the molecular polarizability tensor and enhancement factors that may go beyond physical mechanisms.[22,23] The limitations of these idealizations become clear in the joint SERS and atomic force microscopy (AFM) measurements on single dumbbells that we report. We will find that the structure on finer scale than resolvable through AFM controls the photophysics; moreover, we will find that such structures evolve during irradiation of the junction. As expected, classical fields are inadequate to describe junctions with gaps <5 Å, and in the conductivity limit where Raman reduces to photocurrent scattering on the molecule, reformulation of the observables is necessary.

**Framework for Interpretations.** In the effective medium framework, the dumbbell antenna is considered to be a polarizable medium in which the molecule is embedded. In the dipole coupling limit, the scattering tensor that controls the SERS intensity is

$$\{S_n^2\} = \sum_n |\varepsilon_s^* P^{\mathbf{T}} \beta' R^{\mathbf{T}} \alpha_n' \mathbf{R} \beta P \varepsilon_i|^2 = \sum_n |\mathbf{E}_s^L \alpha_n'(\Omega) \mathbf{E}_i^L|^2 \quad (1)$$

$E_{i,s}^L$ are the enhanced local fields along incidence and scattering directions, $\alpha'$ is the $3 \times 3 \times n$ tensor of polarizability derivatives for the $n$ observable vibrations, and $\Omega = \{\alpha,\beta,\gamma\}$ are the Euler angles that determine the molecular orientation relative to the local fields defined on the dumbbell frame, described by the $R$ rotation matrices; $\boldsymbol{\beta}$ is the matrix of enhancement factors along the principle axes of the dumbbell, $P$ is a $2 \times 3$ projector that transforms the transverse polarization components of the far-field, $\hat{\varepsilon}_{i,s}$, to the image plane. This projection is necessitated because we use high NA objectives, which generate and collect longitudinal field components with phase shift that varies across the focal plane.[24] The essential physics is contained in the $\boldsymbol{\alpha}'$, $\boldsymbol{\beta}$, and $\boldsymbol{\beta}'$ matrices. The polarizability derivative ellipsoid determines the angular resolution of the measurement. Because of the large polarizability associated with $\pi$-conjugated electrons, the DBDT ellipsoid is an elongated cylinder: for all observable modes, $\alpha'_{xx} \gg \alpha'_{yy}, \alpha'_{zz}, \alpha'_{ij}(i \neq j)$, where $x$ defines the long axis of the molecule (see Figure 1). As a result, for a large cone around coaxial alignment of molecule and single applied field, the spectra are indistinguishable. This is illustrated in Figure 1 for a dumbbell irradiated with light polarized along its long axis. Distinct spectra appear when the relative tilt between principle axes exceeds $\varphi = 60°$, with concomitant drop in intensity. Since the linker is chemically bonded, large angle excursions will be accompanied by contraction of the junction gap, which may compensate for variations in orientation-dependent intensity. As such, consistent time histories of spectral intensities contain important information. Our strategy will be to match experimentally observed spectra, to then infer the local fields.

The local fields are displacements given by the sum of applied field and induced polarization: $D = E^0 + 4\pi P$. In the effective polarizable medium, the $E^4$ law of SERS enhancement factors (EF) becomes[25]

$$\mathrm{EF} = \left|\frac{D(v_s)}{E^0}\right|^2 \left|\frac{D(v_i)}{E^0}\right|^2 \quad (2)$$

The elements of the $\beta$ matrices determine the vector components of enhancements:

$$\beta_{ji} = \frac{D_{ji}(v_i)}{|E^0|} = \delta_{ji}(v_i) + \chi_{ji}(v_i)\hat{\varepsilon}_i \quad (3a)$$

$$\beta'_{js} = \frac{D_{js}(v_s)}{|E^0|} = \chi_{js}(v_s)\hat{\varepsilon}_s \quad (3b)$$
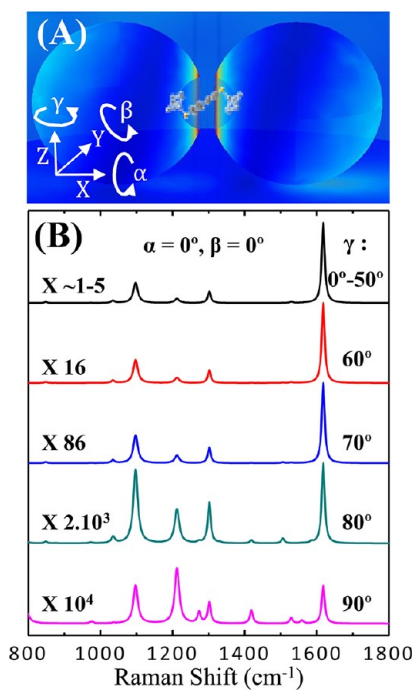
Figure 1. (A) Geometry of dumbbell and the coordinate system used. (B) Raman spectra as a function of rotation angle $\gamma$, along the z-axis, assuming a single enhanced field along the x-axis.
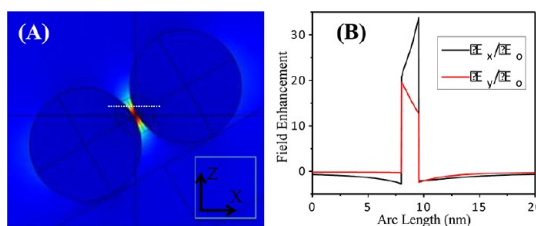


Figure 2. (A) Local fields in the idealized dumbbell junction, for dumbbell tilted at 45° relative to the propagation direction (z) of the excitation laser. (B) Electric field profiles at the nanojunction along the dotted line in (A) show that the local field and field gradient are comparable.

They represent the dielectric response of the dumbbell, in terms of spectral susceptibilities, $\chi_{jo}(v)$. Where appropriate, we rely on numerically computed local fields using FDTD methods.[26] This classical treatment, assumption of linear response, and idealized junction geometries serve only as guides. For junction gaps <5 Å, classical electrodynamics fails.[27] Moreover, the assumption of perfect spheres will prove inadequate. Variations in morphology of the junction can dominate observables.[28,29] A gainful strategy is to initiate a spectral search with local field components based on model considerations, and then carry out an exhaustive search of the Euler space. We compute spectral intensities:

$$I_n(v) \propto (v_i - v_n)^3 v_n^{-1} gf(T) S_n^2 \quad (4)$$

and compare them to intensity normalized spectra: $\Sigma_n I_n = 1$. A faithful reproduction of the observed spectrum determines the vector field experienced by the molecule, described by the field density matrix:

$$\rho(E) = |R(\Omega)\varepsilon_i\rangle\langle\varepsilon_s R(\Omega)| \quad (5)$$

which defines the spectrum: $S_n = \text{Tr}[\alpha'_n \rho(E)]$.

We will find that eq 1 is not sufficient to understand many of the spectra. Both quadrupolar and magnetic dipole Raman scattering, which can be driven by gradients of the enhanced local field,[30] will appear. Even for the idealized dumbbell depicted in Figure 2, the displacement, which defines the effective local field $D_i \equiv E_i^L$, and its linear dispersion are comparable

at the hot spot, $D \sim \langle r\rangle\nabla D$. Therefore, multipolar response cannot be dismissed. Expansion of the polarizability of the dumbbell to first order in spatial dispersion[20]

$$P_i^{(1)}(v, r) = \frac{1}{4\pi}\{[\varepsilon_{ij}(v) - \delta_{ij}]E_j(v, r) + \Gamma_{ijn}^{(1)}\nabla_n E_j(v, r)\} \quad (6)$$

generates the electric dipole−magnetic dipole and electric dipole−electric quadrupole Raman scattering terms. Their squared matrix elements, to lowest order, are given by

$$|S|_m^2 = D_i^* R^T \alpha' R D_s D_s^* R^T G' R M_i \quad (7)$$

$$|S|_q^2 = D_i^* R^T \alpha' R D_s D_s^* R^T A R Q_i \quad (8)$$

$G'$ and $A$ matrices contain the electric dipole−magnetic dipole $G'_{a,b} = \langle\mu_{e,a}\mu_{m,b}\rangle$ and electric dipole−electric quadrupole $A_{a,b,c} = \langle\mu_{e,a}q_{bc}\rangle$ elements,[31] which we compute through the ROA module of Gaussian 09 suite.[32] In eq 7, $M_i$ represents the incident magnetic field vector, $M_{ab} = D_a\partial D/\partial b - D_b\partial D/a$; in (8), $Q_i$ is the incident quadrupole field vector, with three diagonal $Q_{aa}$ and three cross terms $Q_{ab} = D_a\partial D/b + D_b\partial D/\partial\alpha$. The latter only differ from the magnetic terms by the relative phase between displacements. The matrix elements and their numerical evaluation are described in the literature.[33] We have considered a variety of structures to model DBDT attached to two silver spheres and find polarizabilities calculated based on the Ag$_7$−S−DB−S−Ag$_7$ model as an adequate representation of the experiments.[7] The polarizability tensor is computed for the optimized minimum energy structure, in which the staggered phenyl rings impose $D_2$ symmetry on the linker, rendering all of its normal modes to be formally Raman active. The list of the prominent lines, their symmetries, and the explicit transition matrix elements that leads to their observation are given in Table 1 in the Methods section. In the analysis, we only consider overall orientations of the molecule relative to the local field.

**An Uneventful Trajectory: Asperity in the Gap.** In Figure 3, we show a sequence of 35 spectra, consecutively recorded on a single dumbbell, with 10 s acquisition time per spectrum. The set was recorded after

**TABLE 1. Observed and Calculated (B3LYP/def2-TZVP) Vibrational Frequencies and Their Assignments**

| | frequency (cm$^{-1}$) | | assignments | | |
|---|---|---|---|---|---|
| mode # | calculated[a] | experimental | transition[b] | $\Gamma$ ($D_2$)[c] | description |
| 93 | 1580 | 1579 | $R_{xx}$, $M_{yy}$ | A | aromatic C═C stretch coupled to C—C stretch |
| 92 | 1547 | 1548 | $Q_{z,xy}$ | $B_z$ | ring deformation |
| 91 | 1521 | 1516 | $M_{xz}$ | $B_y$ | ring deformation |
| 90 | 1492 | 1493 | $R_{xx}$, $M_{xx}$ | A | HC═CH rock coupled to ring deformation |
| 88 | 1388 | 1380 | $M_{xy}$ | $B_z$ | HC═CH scissor |
| 86 | 1300 | 1298 | $M_{xy}$ | $B_z$ | HC═CH rock |
| 84 | 1271 | 1267 | $[R_{yy}/M_{xz}]^*$ | $[A/B_y]^*$ | C—C stretch combined to C—S—Ag motion |
| 83 | 1243 | 1242 | $M_{xy}$ | $B_z$ | aromatic C═C stretch coupled to H—C rock |
| 81 | 1183 | 1185 | $R_{xx}$ | A | HC═CH dihedral bend |
| 80 | 1163 | 1159 | $[M_{yx}]^*$ | $[B_x]^*$ | HC═CH scissor |
| 77 | 1075 | 1068 | $Q_{x,yz}$ | $B_x$ | C—S stretch coupled to ring expansion |
| 76 | 1071 | 1065 | $R_{xx}$, $M_{yy}$ | A | C—S stretch |
| 75 | 1010 | 994 | $[R_{xx}]^*$ | $[A/B_x]^*$ | in-plane aromatic ring deformation |

[a] The calculation models the system as Ag$_7$—S—DB—S—Ag$_7$, in its minimum energy configuration. The frequencies are scaled using the single scaling factor of 0.9675.
[b] The dominant matrix element in observed scattering processes: SERS, $R_{ab} = \langle \mu_{ea} \mu_{eb} \rangle$; SEMRS, $M_{ab} = \langle \mu_{ea} \mu_{eb} \rangle$; and SEQRS, $Q_{a,bc} = \langle \mu_{ea} \mu_{eb} \rangle$. Note, each of these elements describes only two field—matter interactions. The scattering probabilities are squared quantities, with four field—matter interactions. Our treatment is limited to probabilities given by $|R_{ab}|^2$ for SERS, $R_{ba} M_{ab}$ for SEMRS, $R_{ba} Q_{a,bc}$ for SEQRS. [c] The irreducible representations are for the linker biphenyl with staggered rings, in $D_2$ symmetry. Instead of the more common notation B$_{1/2/3}$ of the asymmetric modes, we have indicated the principle axes by the coordinate system used in Figure 1, hence B$_{x/y/z}$; * indicates modes that do not belong to $D_2$ symmetry, due to involvement of motion along C—S—Ag.

identifying an isolated dumbbell with the AFM and after aligning the polarization of the applied field along its long axis. The field enhancement along this axis dominates by more than a factor of 10 in the idealized dumbbell; therefore, SERS along this direction should be enhanced by more than 10$^4$, rendering all other fields negligible. Indeed, the spectrum consisting of the five totally symmetric A-modes (1577, 1267, 1185, 1065, and 994 cm$^{-1}$; see Table 1) can be reproduced assuming parallel incident and scattered local fields. This, in turn, determines the three Euler angles that define the orientation of the molecule relative to the field (see Figure 3B). Throughout the sequence, the molecule remains confined to the narrow volume in Euler space, $\Omega = \{\alpha, \beta, \gamma\} = \{90 \pm 20°, 0°, 20 \pm 10°\}$. For the ~5 min duration of observation, the molecule behaves as expected for a chemically bound linker at the hot spot of the dumbbell.

In addition to the normal linker spectrum, we see two other lines, at 1496 and 1310 cm$^{-1}$, which appear and disappear uncorrelated in time. DBDT contains a symmetric H—C═C—H rocking mode associated with ring deformation at 1496 cm$^{-1}$ (see Table 1). The intensity of this transition is ~40 times weaker than the main lines when the molecule is aligned with the field. Under the assumption of a single enhanced field component, therefore parallel scattering, $\hat{\varepsilon}_i \hat{\varepsilon}_s = 1$, the observed spectrum cannot be reproduced for any orientation of the molecule. It can only be reproduced if we assume complex field components in both incident and scattered channels. The appearance and disappearance of the 1496 cm$^{-1}$ peak, without changing intensities of the other lines or the overall

intensity of the spectrum, can be accomplished with small reorientations of the molecule subject to the complex fields, $E_i = [1, 0.2i, 1]$ and $E_s = [1, 1, 0.2i]$, as illustrated in Figure 3B. The spectral sensitivity to orientation is remarkable—the observed fluctuation can be accomplished by motion within a 5° cone. The essential ingredients of the observed fluctuation are (a) more than one active enhancement direction and (b) optical activity admitted by the complex fields. Noting that the effect is transient (the spectrum reverts to linear, parallel SERS subject to one field component) and that the molecular orientation is preserved, the structure of the junction must have evolved. Although the vector field density (5) is fully determined by the fit, there is not a trivial mapping to reconstruct a unique local structure. Nevertheless, a sense of the structural change can be obtained by decomposing the spectrum as a sum of parallel and perpendicular scattering: $\beta_{xx}^4 |\hat{\varepsilon}_x \alpha'(\Omega) \hat{\varepsilon}_x|^2 + \beta_{xy}^4 |\hat{\varepsilon}_y \alpha'(\Omega) \hat{\varepsilon}_x|^2$. The first term represents the linker oriented along the long axis of the dumbbell, while in the second term, we find $\Omega' \cong \{0°, 70°, 5°\}$ and $\beta_{xy}/\beta_{xx} \sim 10$; that is, this scattering component is enhanced by a factor of 10 above that of the long axis. Fields along two different directions and different field strengths suggest the formation and disappearance of an asperity with a radius of curvature of $R' \sim R|\beta/\beta'| \sim 3$ nm and oriented along $\Omega'$ relative to the molecule.

We can eliminate several other possibilities. It is not likely that the fluctuation is due to the appearance of a second molecule(s). To observe perpendicular scattering, $\alpha'_{xy}$, two enhanced fields are required, which is not equivalent to two different molecules and a single
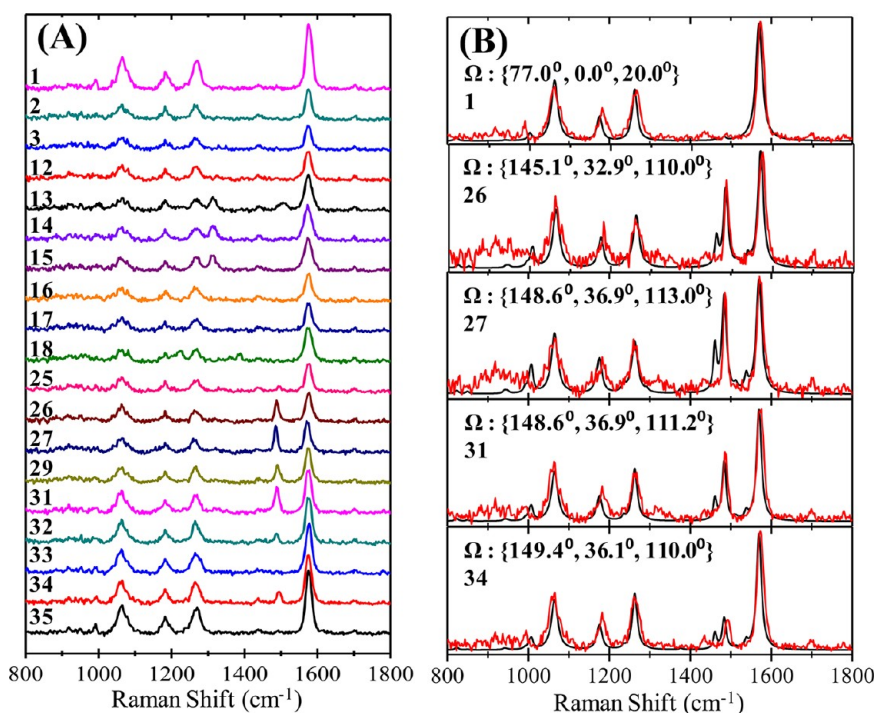
**Figure 3. Uneventful trajectory.** (A) Spectra in a sequence of 35 consecutive acquisitions, with 10 s collection time per acquisition. The prominent spectrum is that of DBDT aligned along the long axis of the dumbbell (compare to Figure 1). The main fluctuation is the highlighted line at 1495 cm$^{-1}$. (B) Fluctuation can be reproduced assuming imaginary field components: $\hat{\varepsilon}_s = [1,0.2i,1]$, $\hat{\varepsilon}_i = [1,1,0.2i]$, and small variations in orientation. The extracted local field density is defined as $|\varepsilon_i R^T(\alpha,\beta,\gamma)\rangle\langle R(\alpha,\beta,\gamma)\varepsilon_s|$, at rotation angles indicated in the figure.

field. Also, the absence of correlation between this single line fluctuation and the rest of the spectrum would be difficult to rationalize for two independent scattering centers, $c_1 l_1 + c_2 l_2$, since in all lines there would have to be the conservation principle that $c_1 + c_2 = 1$. We have considered the possibility that the fluctuation is an attempt by the molecule to walk, as seen for dithiols through scanning tunneling microscopy.[34] To this end, we have considered both homolytic and heterolytic cleavage of one S—Ag bond, to produce the radical Ag—S—DB—S or the anion Ag—S—DB—S$^-$. In the radical, the C=C ring modes split, while in the anion the entire peak red shifts. Although many features are common to all three spectra, a satisfactory match cannot be obtained for one-sided linkage.

We cannot account for the 1310 cm$^{-1}$ line in the present model. It appears to be a splitting of the in-plane C—H vibrations. In the staggered geometry, these modes can be regarded as those of a pair of poorly coupled phenyl rings, therefore nearly degenerate pairs. Upon twisting to coplanarity, they should couple and split. This expectation was not borne out in computed spectra as a function of twist angle. Instead, we see shifts and splittings of vibrations that are coupled to the C—S—Ag motion (see Table 1). The failure of the analysis to account for changes in vibrational frequency highlights its limitations. Because the molecular geometry is frozen in the treatment, it

cannot account for spectral shifts or splittings. Finally, there are minor spectral features that are unaccounted, which are extraneous to DBDT. The binder on the silver spheres and the polymer film on the slide are the most likely contributors. In addition to their smaller Raman cross sections, we reason that they are not more prominent because of the synthetic strategy. For the spheres to be linked by a 1 nm long molecule, the facets must be relatively clear of other species.

**As the Spheres Fuse.** We consider a sequence of SERS spectra recorded during the fusion of the nanospheres. The AFM images of the dumbbell before and immediately after recording the sequence are shown in Figure 4. The fusion is light-induced,[35] initiated by the poor anchoring of the dumbbell in the PVA film. Otherwise, the irradiation intensity ($\sim$1 mW/$\mu$m$^2$) is the same as in the first sequence. The image plot of Figure 5 shows the consecutively recorded spectra, at 10 s acquisition per spectrum. Selected spectra are shown in Figure 5B and Figure 6B. The contrast with the trajectory of Figure 3 is stark. Dramatic variations occur in overall intensity, in relative intensities, and a reversible transition from line spectrum to banded spectrum is observed. In addition to DBDT, a line appears at 2115 cm$^{-1}$, characteristic for atop chemisorption of CO on silver.[36–40] CO is most likely derived from the PVA film, analogous to demonstrations of irradiated carbon clusters on roughened silver or gold where generation of CO at plasmonic hot spots is seen.[41] At room
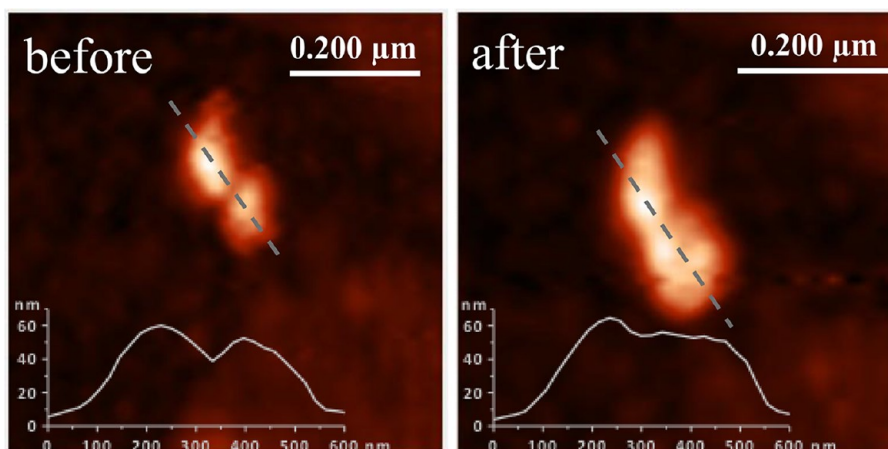
**Figure 4.** AFM images of the dumbbell before and after recording the SERS sequence. The resolution is sufficient to identify the isolated dumbbell and its principal axis for the purpose of aligning the polarization of the incident field. As the junction fuses during the measured sequence, the effective intersphere distance becomes negative.
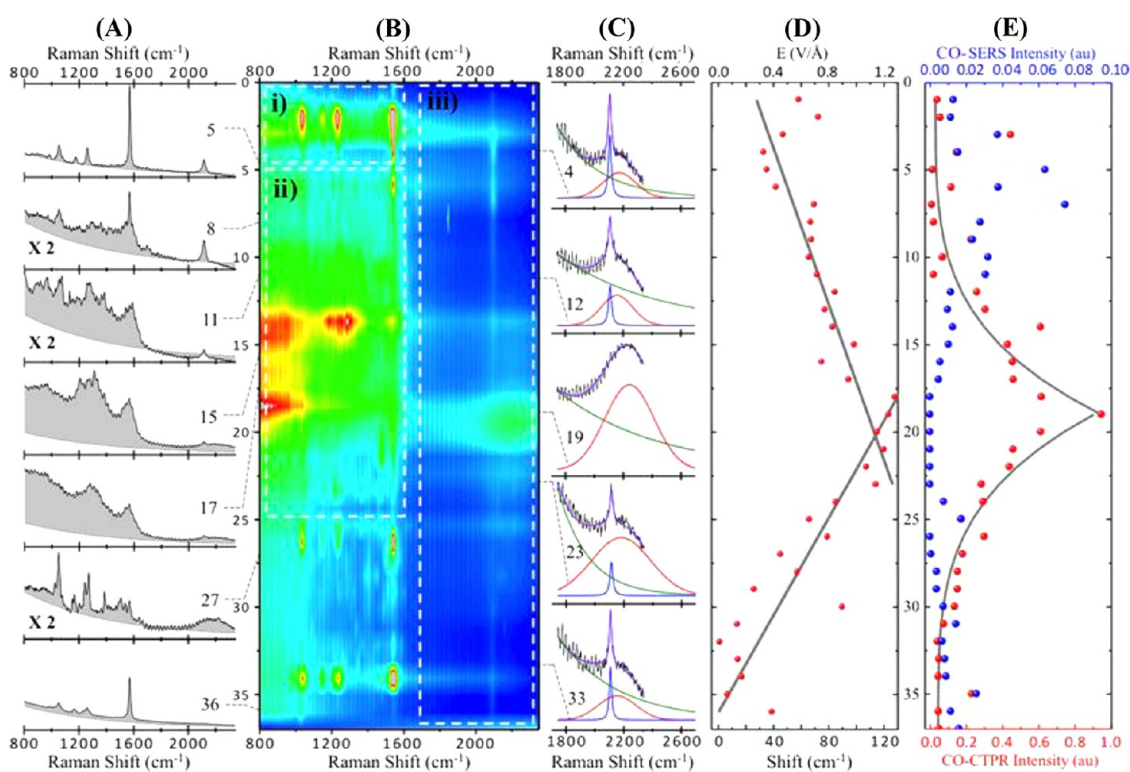


**Figure 5.** (A) Image plot of a sequence of 36 SERS spectra recorded consecutively, during the fusion of the dumbbell. The white squares highlight (i) 50-fold fluctuation in overall intensity of the normal SERS line spectrum, ascribed to tuning across the BDP resonance by the closing junction; (ii) development of band spectra and a dramatic increase in integrated intensity, assigned to the transition to the conductivity limit where current passing though the molecule leads to Stark shifting and broadening. (c) CO spectral region, which shows evolution that parallels but trails that of DBDT. (B) Selected spectra from the image plot: #5, SERS line spectrum of DBDT and CO; #8, onset of band spectrum at the DBDT site, while the normal SERS of CO is observed; #15 and #17, dominance of band spectra at both sites; #27, re-emergence of lines at the DBDT site, while CO remains in the CTP regime; #36, normal SERS line spectrum of DBDT, where the molecule is now outside the conductivity range of the spheres and appears unscathed by the fusion process. (C) Decomposition of the CO spectrum into the normal SERS line at 2115 cm$^{-1}$ and the broad CTPR band with evolving band center. (D) Sequential spectral shift of the CO charge transfer resonance (bottom abscissa), and the associated Stark field (top abscissa). The shift reaches a limiting value of ~100 cm$^{-1}$, which corresponds to 1 V/Å. (E) Intensity of the normal CO SERS line (blue) and the CTPR band (red). Note the 10-fold difference in scales. The curves are the fourth power of the local field obtained from the spectral shift in (D).

temperature, CO only binds to unsaturated surface atoms of noble metals, as rigorously demonstrated through particle-size-dependent desorption measurements on gold.[42] We can be sure that CO is attached to an atomically sharp asperity in the junction; otherwise, it would desorb. Moreover, once formed, we can be sure that the
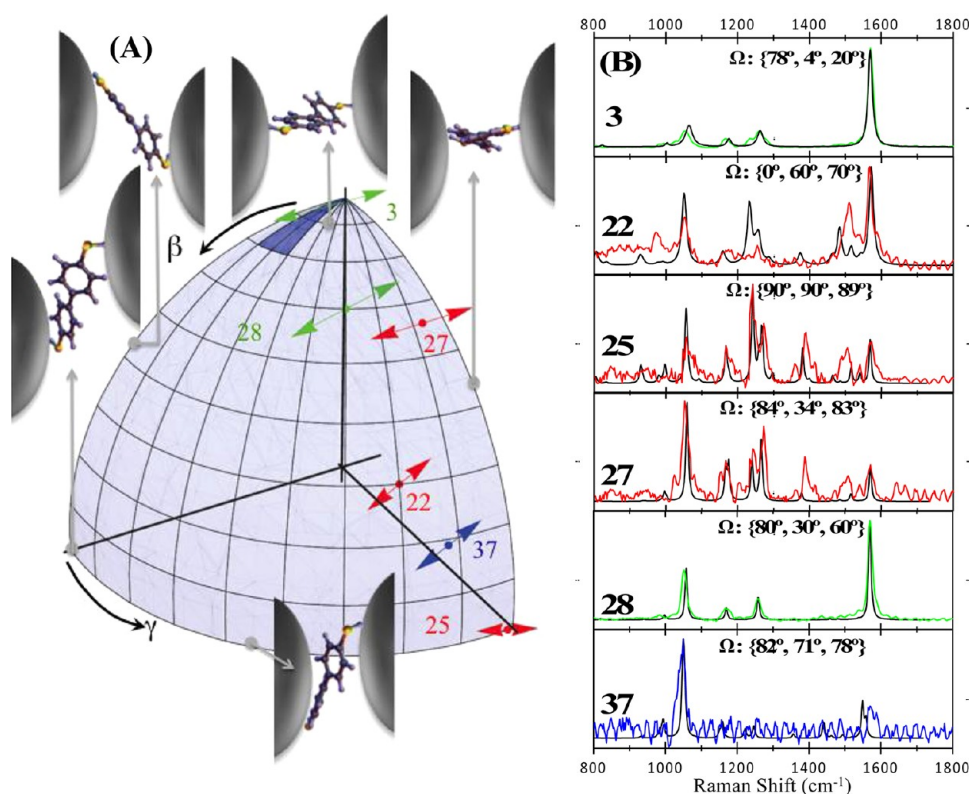
**Figure 6.** (A) SERS trajectory in Euler space. The polar and azimuthal angles are relative to the dumbbell frame, while the orientation of the double-sided arrows indicates rotation of the molecular plane relative to its principal axis. Structures are shown at selected angle to visualize the molecule junction orientation. Note, the full length of the molecule is 11 Å; the orientations make it clear that the junction hovers between contact and ~5 Å. The color code is matched with the spectral reproductions in panel B. (B) Spectral matches are color-coded to identify the Raman scattering process as dipolar (green), dipole−magnetic dipole (red), and dipole−quadrupole (blue) at the indicated Euler angles.

temperature at the CO site does not exceed ~350 K. Therefore, the fusion sequence we follow is not due to melting, but rather driven by the polarization forces at the hot spot.[36] The vibrational frequency of CO is sensitive to its adsorption site, and interacting CO molecules, such as can be generated at high surface coverage, red shift and develop a broad red band.[39] Here, a broad blue-shifted band appears with intensity anticorrelated to the normal SERS line of CO. We will assign the blue band, which shows the characteristic Stark shift of CO, to the charge transfer plasmon resonance (CTPR).

The assignable spectra of DBDT (Figure 6B) determine the trajectory of the molecule in Euler space (Figure 6A). The molecular orientation spans the full Euler space. The trajectory starts in the normal linker orientation (#1−5) and reaches the vertical plane bisecting the fusing nanospheres (#28). In addition to normal Raman, in which all four field interactions are dipole-coupled (Table 1 footnote), we see spectra in which one of the fields is either quadrupole (SEQRS) or magnetic dipole coupled (SEMRS). These appear before and after the broadening of lines seen in spectra #11−20 of the sequence in Figure 5. Searches of the Euler space establish that the SEMRS is dominated by a magnetic field along the z-axis, while the SEQRS is due to the $q_{xx}$ quadrupole. Both the intensities and

directions of these scattering components are difficult to understand in terms of field gradients alone. For example, the SEQRS, which is dominated by two lines (Figure 6B), makes it clear that this is not a minor component of the overall scattering, but rather the only component. The switch from normal dipolar Raman to SEQRS can be understood as the tuning of field plasmon resonances. At junction gaps of $d \sim 1-2$ Å, the dipolar plasmon shifts to the IR and the binding $q_{xx}$ quadrupolar plasmon (BQP) come into resonance with the excitation laser (at 2.3 eV).[12,13] Indeed, the entire spectral sequence is most consistently explained by recognizing that plasmon resonances tune through the fixed excitation frequency as the spheres fuse, and this determines the observable elements of the Raman tensor. This applies to both DBDT and CO spectra, as we expand below.

During the first 50 s sequence (Figure 5, #1−5), the intensity of the entire normal DBDT spectrum breathes by a factor of ~50. The implied fluctuation in the local field is a factor of $2.5 \sim 50^{1/4}$. During this episode, the spectrum is strictly dipolar SERS (see #5 in Figure 5B). Since the linker starts at the hot spot, aligned along the largest field, the increase in local field must be associated with the tuning of the plasmon resonance by contraction of the junction. This can be accomplished by the approaching crevice of fusing spheres. Thus, for

30 nm silver spheres separated by 1 nm, we calculate an enhancement factor of $\beta_{xx} = 40$. At the crevice of a fused pair of spheres, 1 nm removed from the contact point, we calculate $\beta_{xx} = 90$, which is reasonably consistent with the observed intensity fluctuation. The crevice must recede for the intensity to revert. Alternatively, and more consistent with the full history, the intensity fluctuation can be understood as the tuning-in of the bonding dipolar plasmon (BDP) resonance as the intersphere gap contracts. At 532 nm, the excitation is to the red of the dipolar plasmon resonance for perfect silver spheres separated by 1 nm.[7] The resonance red shifts as the gap closes.[12,13] Note, the AFM determined shape of the dumbbell after fusion is equivalent to a negative gap; that is, the shape corresponds to that of overlapping spheres. Accordingly, the sequence captures the crossover region where the effective gap distance changes sign and the BDP resonance tunes down to zero frequency. In the process, the BDP resonance must necessarily pass through 532 nm, and this would explain the fluctuation in overall intensity of the normal Raman spectrum.

The episode of overall intensity fluctuation is followed by the transition to band spectra (#12−20) in which only the parentage of DBDT lines is apparent. The integrated intensity under the band spectra is an order of magnitude larger than the most intense line spectrum seen in the sequence. We associate the onset of band spectra with the transition to the conductivity limit.[43] In this limit, the field plasmons are shorted by the current carrying CTP, Raman scattering is accompanied by photocurrent passing through the molecule, and vibrational resonances can be expected to broaden *via* inelastic electron scattering. Note, after embedding in the junction, the molecule reappears unscathed (#36); therefore, the confining junction of the molecule reopens. Characteristically, the multipolar Raman spectra appear at the transition from line spectra to band spectra. As the junction reopens, we first see SEMRS (#22−25), then the normal Raman spectrum of the molecule in the vertical plane (#28), then the normal linker spectrum in the horizontal plane (#36), followed by the SEQRS (#37) before the molecule is lost from sight. The fusion sequence appears to track the tuning of plasmonic resonances. As the gap distance passes through zero and assumes effective negative values, the BDP, BQP, and CTP resonances should scan sequentially through the excitation wavelength.[12,13] This nicely explains the sequence of dipolar Raman, multipolar Raman, and band spectra (#1−20) and the reversal of the process in the same order (#20−36).

**CO as a Gauge of Local Fields.** The above picture is re-enforced and quantified by the CO spectra, the evolution of which trails that of DBDT. The faint SERS of CO appears as the DBDT line spectrum reaches its maximum intensity (#3), which we associated with the gap-tuned BDP resonance. The intensity of the CO line peaks (#4) and after fluctuating, it decays while its blue-shifted CTPR band grows. The anticorrelated history of the SERS line *versus* CTPR band is quantified by decomposing the spectrum into two components (Figure 5C). The extracted peak shift of the CTPR and integrated intensities of SERS and CTPR are plotted in Figure 5D,E. As the SERS intensity decays to zero, the CTPR intensity builds up to its maximum value, to an integrated intensity that is an order of magnitude larger than that of the SERS line (see Figure 5E). The process reverses: the band intensity decays and the SERS line reappears. The CTPR band shifts linearly while its intensity grows exponentially, and both spectral shift and intensity reverse sign at the same time (Figure 5D,E). The sequence identifies the closing and reopening of the junction at the CO site. The contact point is sharply defined in the case of CO, to be contrasted with the DBDT where the band spectra evolve more gradually, reflecting the contortions of the molecule (Figure 6A) as the gap closes.

The CTP resonance is consistent with its assignment to SERS when current is passing through the molecule. Since CO is subject to a first-order Stark shift of $10^2$ cm$^{-1}$ (V/Å)$^{-1}$,[44,45] we can deduce the local field experienced by it. The peak shift indicates a DC field, while the peak width ($300 \pm 50$ cm$^{-1}$ throughout) should be determined by the combination of AC Stark shift and dephasing. Since the junction is asymmetric, due to one-sided chemisorption of CO, it should lead to rectification of the optical field.[46] The peak shift is used to construct the secondary axis in Figure 5D. The field reaches a limiting value of 1.1 V/Å, therefore a chemical potential across the 1.1 Å bond length of CO of 1.2 eV. As a single channel conductor, the photocurrent passing through the molecule would be subject to the quantum of conductance $G_0 = 2e^2/h = 7 \times 10^{-5}$ $\Omega^{-1}$. Consistent with this, the limiting current $J = VG_0 = 0.07$ mA, which equals $4 \times 10^{14}$ $e^-$/s, corresponds to the transfer of one electron per vibrational cycle of CO: $\omega = 3.95 \times 10^{14}$ cycles/s (2100 cm$^{-1}$). While the spectral shift is linear with time, the accompanying intensity of the CTPR is highly nonlinear and holds important clues regarding to the nature of the enhanced scattering process. Identifying the Raman scattering intensity with the transition current $I \sim E_L^4 \langle u\omega \rangle^4 \sim E_L^4 \langle J \rangle^4$, we may expect it to evolve at least with the fourth power of the local field, which is indicated in Figure 5E. This ignores the field dependence of the current, $\langle J \rangle$, which if associated with photo-field-induced tunneling, then an exponential dependence on junction gap and field would be expected. Indeed, the observed intensity dependence can be better fit to an exponential. Closer inspection of the intensity shows a symmetric staircase about the peak, suggestive of quantized conductance channels as seen in

break junctions.[47] The conductance should be determined by the number of contacts between silver atoms during the closing of the junction. In contrast with the field measured by the vibrational shift, which gauges current passing through CO, the intensity should be determined by the photocurrent sustained across the entire fusing junction. In effect, the Ag−CO−Ag contact is an asymmetric metal−insulator−metal tunnel junction, which corresponds to a rectifying photodiode.[48] The plasmonic nature of the junction boosts its photocollection efficiency, by endowing it with a frequency-tunable antenna.[49] It should be appreciated that an asymmetric plasmonic junction in the conductivity limit combines all of the design elements for an ideal photocollector.[49] We will expand on the photoconductivity of such junctions elsewhere. Here, we focus on light scattering.

The determination of the local field by the Stark shift allows a direct measure of SERS enhancement factors. Given the irradiation intensity of 1 mW/$\mu m^2$ (8.6 × $10^{-4}$ V/Å), to reach 1 V/Å, the field must be enhanced by $E/E_0 = 1.1 \times 10^3$, with associated Raman enhancement factor in excess of EF = $(E/E_0)^4 = 10^{12}$. Such enhancement is necessary to see a single CO molecule in SERS given its Raman cross section of 3.3 × $10^{-31}$ $cm^2$/sr,[50] which is nearly 3 orders of magnitude smaller than that of DBDT. Evidently, within the same nanojunction, the local field experienced by CO is nearly 10 times larger than by DBDT: CO must be chemisorbed on an atomically terminated sharp protrusion, which we deduced based on the requirement for chemisorption at room temperature.[42] Previously, ensemble measurements of SERS of CO have been used to associate spectra with local structure.[41] The large enhancements we ascribe to a protrusion within the hot spot of the dumbbell is contained in the fractal structures considered in the interpretation of SERS on colloidal preparations.[51]

The field-induced blue shift of the CO band is informative. The Stark shift of CO chemisorbed on metals has been analyzed.[52,53] The blue shift arises at positive applied potentials, as a combination of electrostatic shift and reduction of $\pi^*$ back-donation from the metal d electrons. The shift suggests a net depletion of back-donated electrons during the CTP excitation, which involves electrons near the Fermi edge.[54,55] Given the short dephasing time of the CTP, the observed line width should be determined by nonadiabatic evolution on the ground vibronic state, common to damping of molecular vibrations on metal surfaces.[56,57] The contrast between SERS and CTPR is significant. On the basis of the 30 $cm^{-1}$ width of the normal SERS line, the observed vibrational dephasing time of CO is 1.1 ps, in line with prior measurements[58,59] and typical for CO chemisorbed on metal surfaces.[60] The dephasing time of the CTPR band is 100 fs, on the time scale of electron−phonon scattering in metals. The contrast

seems less dramatic if we consider vibrational dephasing by the local density of electrons, $1/\tau = \pi\omega(\delta n)^2/2$, where $\delta n$ is the fluctuation in the number of back-donated d−$\pi^*$ electrons:[56] $\delta n = 0.02$ would explain the normal SERS line, while the CTPR lifetime would suggest a 3-fold increase: $\delta n = 0.06$ electrons. This may be a reflection of the fact that d electrons in silver are deeply buried,[40] while the current in CTP is principally carried by the sp electrons at the Fermi edge[12] with the $\pi^*$ orbital of CO acting as a conductive bridge.

## CONCLUSIONS

Consistent with our prior analysis, the presented SERS trajectories suggest that we are observing a single molecule on a single nano-dumbbell. The trajectories illustrate the concept of tracking a single molecule in 3D space, in the inhomogeneous local field of a nanojunction. The motions we follow are sluggish, matched with the data collection time of a frame per 10 s. Principally, they involve the restructuring of the junction. We have seen the appearance and disappearance of an asperity nearby the molecule, a process that leads to surface-enhanced Raman optical activity—linearly polarized excitation leads to elliptic excitation and scattering due to substructure of the junction. This underscores the challenge in interpreting polarization-dependent SERS measurements.[7,61]

The fusion sequence interrogates the full range of plasmonic activity at a nanojunction and the evolution of spectral response during the field to current transition of the junction plasmon. The principle motion in this sequence is the closing and reopening of the gap, at the gentle pace of ~1 Å/min. The gap, which may not exceed the S−S separation of the linker of 11 Å, can be gauged by the Euler space trajectory of the molecule (Figure 6). At contact with CO, the physical gap would be limited by its bond length of 1.1 Å. However, the effective intersphere distance assumes negative values as the neck of the junction widens. In the process, we observe the sequential evolution of the Raman spectra of the linker from dipolar SERS, to SEQRS and SEMRS, to intense band spectra, tracking the predicted spectral evolution of the dumbbell plasmon from BDP, to BQP, to CTP as a function of gap distance. The assigned multipolar spectra identify some of the origins of fluctuations and blinking seen in single-molecule SERS. We identify the crossover to the conduction limit as the transition from line to band spectra. In the case of CO, the normal SERS line converts to a broad blue-shifted band, subject to first-order Stark effect. The spectral shifts of the bands in DBDT are smaller and typically red shaded. In the absence of a permanent dipole, DBDT is subject to second-order Stark shift, $\Delta\upsilon \propto \alpha' E^2/2$, therefore mode-specific and quadratic in the field. This provides an explanation for some of the continua

observed in SERS, the origin of which has been extensively deliberated.[62−64] The CTPR continua are distinct from broadened Rayleigh, in which electron−hole pair excitation of the metal leads to scattering on defects and surface states and leads to a tail originating at the excitation origin.[65] Mechanistically, the CTPR continua fit the model of ballistic electron−hole scattering on interfacial molecules.[66] The compelling assignments of spectra and mechanisms in the present derive from the engineered nanostructure and the requirement of consistency of histories imposed by single-molecule

trajectories. The same applies to the observation of CO chemisorption on an asperity, which otherwise is difficult to recognize in ensemble measurements. We expect quantitative treatments of these prototypical systems to be possible with the development of its essential ingredients: coupled molecule−plasmon dynamics and light scattering in current-carrying junctions.[67] Beside fundamental motivations, it may be recognized that CTPR in an asymmetric phototunneling junction combines the ideal design elements of a photovoltaic cell, namely, the rectenna design.[68]

## METHODS

**Experimental.** The synthetic strategy to prepare the nanodumbbells has been reported previously.[69] Briefly, a colloidal suspension of 35 ± 5 nm citrate-capped silver nanospheres is prepared with a narrow size distribution. The citrate is then exchanged with bis(p-sulfonatophenyl)phenylphosphine, which serves as a protective capping agent. A 1 mM DBDT solution is added to the suspension, allowed to sit for ~3 h, followed by centrifugation. The resulting solution consists of ~50% nanosphere dimers, which is characterized by transmission electron microscopy. The strategy ensures that the linker is at the hot spot of the nanosphere dimer but does not guarantee that the dumbbell is assembled by one linker alone.

Joint AFM/Raman measurements are carried out under ambient conditions, on dry mounted dumbbells prepared by spin-coating or drop-casting a ~5 pM solution on a 150 $\mu$m thick microscope slide.[7] A dilute solution of polyvinyl alcohol (PVA) is added to the aqueous suspension prior to coating, and the slides are either preheated or heat cycled on a hot plate after preparation. The polymer film provides the mechanical stability required for AFM imaging and serves as the essential heat sink for thermal stability. The AFM resolution is limited. It serves to identify dumbbells that are isolated in the field of view of the high NA objective and serves to identify the orientation of the dumbbell to align the polarization of the laser with a half-wave plate. The excitation source is a continuous wave, single mode laser operating at $\lambda = 532$ nm. A 1.25 NA oil immersion lens is used to focus the laser on the sample and to collect the back-scattered Raman light through a pair of notch filters (Semrock, 1:10$^6$ extinction). The spatially filtered scattered light is spectrally dispersed in a 0.25 m monochromator and recorded on a CCD array (Andor, V401-BV). The effective instrument resolution is 10 cm$^{-1}$.

**Computational.** Calculations were performed using the methodologies implemented in Gaussian 09. The system is modeled as DBDT attached to seven silver atoms on either side: Ag$_7$−S−DB−S−Ag$_7$.[7] Unconstrained geometry optimization was performed using the B3LYP functional.[70] The final calculations employ the def2-TZVP basis set[71] with matching pseudo-potentials for silver (>1000 basis functions). The optimized structures are verified to not have imaginary vibrational frequencies. The polarizability tensors are obtained using the ROA module in Gaussian 09. In the relaxed geometry, the phenyl groups of DBDT are staggered. The symmetry of the linker (ignoring silver atoms) is reduced to $D_2$; therefore, all 60 of its normal modes are formally Raman active. In Table 1, we list the prominent lines observed in the spectra, their symmetry classification in $D_2$, and the matrix elements of the transitions observed. Note, inclusion of the silver atoms into consideration (a total of 102 normal modes are computed) further reduces the symmetry to $C_s$. Accordingly, modes that entail significant C−S−Ag motion (indicated by * in Table 1) cannot be classified under $D_2$ and are sensitive to the assumed chemisorption model.

*Conflict of Interest:* The authors declare no competing financial interest.

## REFERENCES AND NOTES

1. Le Ru, E.; Etchegoin, P. G. Single-Molecule Surface-Enhanced Raman Spectroscopy. *Annu. Rev. Phys. Chem.* **2012**, *63*, 65–87.
2. Kreibig, U.; Vollmer, M. *Optical Properties of Metal Clusters*; Springer-Verlag: Berlin, 2006.
3. Gunnarsson, L.; Rindzevicius, T.; Prikulis, J.; Kasemo, B.; Käll, M.; Zou, S.; Schatz, G. C. Confined Plasmons in Nanofabricated Single Silver Particle Pairs: Experimental Observations of Strong Interparticle Interactions. *J. Phys. Chem. B* **2005**, *109*, 1079–1087.
4. Encina, E. R.; Coronado, E. A. Plasmon Coupling in Silver Nanosphere Pairs. *J. Phys. Chem. C* **2010**, *114*, 3918–3923.
5. Nordlander, P.; Oubre, C.; Prodan, E.; Li, K.; Stockman, M. I. Plasmon Hybridization in Nanoparticle Dimers. *Nano Lett.* **2004**, *4*, 899–903.
6. Whitmore, D.; El-Khoury, P. Z.; Fabris, L.; Chu, P.; Bazan, G. C.; Potma, E. O.; Apkarian, V. A. High Sensitivity Surface-Enhanced Raman Scattering in Solution Using Engineered Silver Nanosphere Dimers. *J. Phys. Chem. C* **2011**, *115*, 15900–15907.
7. Banik, M.; Nag, A.; El-Khoury, P. Z.; Perez, A. R.; Guarrotxena, N.; Bazan, G. C.; Apkarian, V. A. Surface-Enhanced Raman Scattering of a Single Nanodumbbell: Dibenzyldithio-Linked Silver Nanospheres. *J. Phys. Chem. C* **2012**, *116*, 10415–10423.
8. Kedziora, G. S.; Schatz, G. C. Calculating Dipole and Quadrupole Polarizabilities Relevant to Surface Enhanced Raman Spectroscopy. *Spectrochim. Acta, Part A* **1999**, *55*, 625–638.
9. Romero, I.; Aizpurua, J.; Bryant, G. W.; García-Vidal, F. Plasmons in Nearly Touching Metallic Nanoparticles: Singular Response in the Limit of Touching Dimers. *Opt. Express* **2006**, *14*, 9988–9999.
10. Lassiter, J. B.; Aizpurua, J.; Hernandez, L. I.; Brandl, D. W.; Romero, I.; Lal, S.; Hafner, J. H.; Nordlander, P.; Halas, N. J. Close Encounters between Two Nanoshells. *Nano Lett.* **2008**, *8*, 1212–1218.
11. Pérez-González, O.; Zabala, N.; Aizpurua, J. Optical Characterization of Charge Transfer and Bonding Dimer Plasmons in Linked Interparticle Gaps. *New J. Phys.* **2011**, *13*, 083013–083029.
12. Marinica, D. C.; Kazansky, A. K.; Nordlander, P.; Aizpurua, J.; Borisov, A. G. Quantum Plasmonics: Nonlinear Effects in the Field Enhancement of a Plasmonic Nanoparticle Dimer. *Nano Lett.* **2012**, *12*, 1333–1339.
13. Esteban, R.; Borisov, A. G.; Nordlander, P.; Aizpurua, J. Bridging Quantum and Classical Plasmonics with a Quantum-Corrected Model. *Nat. Commun.* **2012**, *3*, 1–9.

14. Jensen, L. Surface-Enhanced Vibrational Raman Optical Activity: A Time-Dependent Density Functional Theory Approach. *J. Phys. Chem. A* **2009**, *113*, 4437–4444.

15. Kneipp, H.; Kneipp, J.; Kneipp, K. Surface-Enhanced Raman Optical Activity in Silver Colloidal Solution. *Anal. Chem.* **2006**, *78*, 1363–1366.

16. Abdali, S. Observation of SERS Effect in Raman Optical Sctivity, a New Tool for Chiral Vibrational Spectroscopy. *J. Raman Spectrosc.* **2006**, *37*, 1341–1345.

17. Acevedo, R.; Lombardini, R.; Halas, N. J.; Johnson, B. R. SEROA. *J. Phys. Chem.* **2009**, *113*, 13173–13183.

18. Etchegoin, P. G.; Galloway, C.; Le Ru, E. C. Polarization-Dependent Effects in Surface-Enhanced Raman Scattering (SERS). *Phys. Chem. Chem. Phys.* **2006**, *8*, 2624–2628.

19. Wilson, E. B.; Decius, J. C.; Cross, P. C. *Molecular Vibrations: The Theory of Infrared and Raman Vibrational Spectra*; Dover: New York, 1980.

20. Svirko, Y. P.; Zheludev, N. I. *Polarization of Light in Non-linear Optics*; Wiley: New York, 1998.

21. Nie, S.; Emory, S. R. Probing Single Molecules and Single Nanoparticles by Surface-Enhanced Raman Scattering. *Science* **1997**, *275*, 1102–1106.

22. Morton, S. M.; Jensen, L. Understanding the Molecule-Surface Chemical Coupling in SER. *J. Am. Chem. Soc.* **2009**, *131*, 4090–4098.

23. Lombardi, J. R.; Birke, R. L. A Unified View of Surface-Enhanced Raman Scattering. *Acc. Chem. Res.* **2009**, *42*, 734–742.

24. Novotny, L.; Hecht, B. *Principles of Nano-Optics*; 1st ed.; Cambridge University Press: New York, 2011.

25. Le Ru, E. C.; Etchegoin, P. G. Rigorous Justification of the $|E|^4$ Enhancement Factor in Surface Enhanced Raman Spectroscopy. *Chem. Phys. Lett.* **2006**, *423*, 63–66.

26. We use the Comsol Multiphysics (ver. 4.2) code for the simulations.

27. Zuloaga, J.; Prodan, E.; Nordlander, P. Quantum Description of the Plasmon Resonances of a Nanoparticle Dimer. *Nano Lett.* **2009**, *9*, 887–891.

28. Luo, Y.; Pendry, J. B.; Aubry, A. Surface Plasmons and Singularities. *Nano Lett.* **2010**, *10*, 4186–4191.

29. Luo, Y.; Lei, D. Y.; Maier, S. A.; Pendry, J. B. Transformation-Optics Description of Plasmonic Nanostructures Containing Blunt Edges/Corners: From Symmetric to Asymmetric Edge Rounding. *ACS Nano* **2012**, *6*, 6492–6506.

30. Ayars, E. J.; Hallen, H. D.; Jahncke, C. L. Electric Field Gradient Effects in Raman Spectroscopy. *Phys. Rev. Lett.* **2000**, *85*, 4180–4183.

31. Buckingham, A. D.; Dunn, M. B. Optical Activity of Oriented Molecules. *J. Chem. Soc. (A)* **1971**, 1988–1991.

32. Frisch, M. J.; Trucks, G. W.; Schlegel, H. B.; Scuseria, G. E.; Robb, M. A.; Cheeseman, J. R.; Scalmani, G.; Barone, V.; Mennucci, B.; Petersson, G. A.; et al. *Gaussian 03*, revision C02; Gaussian Inc.: Pittsburgh, PA, 2003.

33. Ruud, K.; Helgaker, T.; Bour, P. Gauge-Origin Independent Density-Functional Theory Calculations of Vibrational Raman Optical Activity. *J. Phys. Chem. A* **2002**, *106*, 7448–7455.

34. Kwon, K.-Y.; Wong, K.; Pawin, G.; Bartels, L.; Stolbov, S.; Rahman, T. Unidirectional Adsorbate Motion on a High-Symmetry Surface: "Walking" Molecules Can Stay the Course. *Phys. Rev. Lett.* **2005**, *95*, 166101–166104.

35. Hallock, A.; Redmond, P. L.; Brus, L. E. Optical Forces between Metallic Particles. *Proc. Natl. Acad. Sci. U.S.A.* **2005**, *102*, 1280–1284.

36. Dilella, D. P.; Gohin, A.; Lipson, R. H.; Mcbreen, P.; Moskovits, M. Enhanced Raman Spectroscopy of CO Adsorbed on Vapor-Deposited Silver. *J. Chem. Phys.* **1980**, *73*, 4282–4295.

37. Abe, H.; Manzel, K.; Schulze, W.; Moskovits, M.; Dilella, D. P. Surface-Enhanced Raman Spectroscopy of CO Adsorbed on Colloidal Silver Particles. *J. Chem. Phys.* **1981**, *74*, 792–797.

38. Seki, H. SERS Excitation Profile of Pyridine and CO on Silver in UHV. *J. Electroanal. Chem.* **1983**, *150*, 425–436.

39. Dumas, P.; Tobin, R. G.; Richards, P. L. Study of Adsorption States and Interactions of CO on Evaporated Noble Metal Surfaces by Infrared Absorption Spectroscopy: I. Silver. *Surf. Sci.* **1986**, *171*, 555–578.

40. Föhlisch, A.; Nyberg, M.; Hasselström, J.; Karis, O.; Pettersson, L. G.; Nilsson, A. How Carbon Monoxide Adsorbs in Different Sites. *Phys. Rev. Lett.* **2000**, *85*, 3309–3312.

41. Kudelski, A.; Pettinger, B. Fluctuations of Surface-Enhanced Raman Spectra of CO Adsorbed on Gold Substrates. *Chem. Phys. Lett.* **2004**, *383*, 76–79.

42. Lemire, C.; Meyer, R.; Shaikhutdinov, S. K.; Freund, H.-J. CO Adsorption on Oxide Supported Gold: From Small Clusters to Monolayer Islands and Three-Dimensional Nanoparticles. *Surf. Sci.* **2004**, *552*, 27–34.

43. Atay, T.; Song, J.-H.; Nurmikko, A. V. Strongly Interacting Plasmon Nanoparticle Pairs: From Dipole−Dipole Interaction to Conductively Coupled Regime. *Nano Lett.* **2004**, *4*, 1627–1631.

44. Lambert, D. K. Observation of the First-Order Stark Effect of Co on Ni(110). *Phys. Rev. Lett.* **1985**, *50*, 2106–2109.

45. Lambert, D. K. Vibrational Stark Effect of Adsorbates at Electrochemical Interfaces. *Electrochim. Acta* **1996**, *41*, 623–630.

46. Sanchez, A.; Davis, C. F.; Liu, K. C.; Javan, A. The MOM Tunneling Diode: Theoretical Estimate of Its Performance at Microwave and Infrared Frequencies. *J. Appl. Phys.* **1978**, *49*, 5270–5277.

47. Krans, J. M.; Van Rultenbeek, J. M.; Fisun, V. V.; Yanson, I. K.; De Jongh, L. J. The Signature of Conductance Quantization in Metallic Point Contacts. *Nature* **1995**, *375*, 767–769.

48. Hobbs, P. C. D.; Laibowitz, R. B.; Libsch, F. R. Ni−NiO−Ni Tunnel Junctions for Terahertz and Infrared Detection. *Appl. Opt.* **2005**, *44*, 6813–6822.

49. Choi, K.; Yesilkoy, F.; Ryu, G.; Cho, S. H.; Goldsman, N.; Dagenais, M.; Peckerar, M. A. Focused Asymmetric Metal−Insulator−Metal Tunneling Diode: Fabrication, DC Characteristics and RF Rectification Analysis. *IEEE Trans. Electron Devices* **2011**, *58*, 3519–3528.

50. Hyatt, H. A.; Cherlow, J. M.; Fenner, W. R.; Porto, S. P. S. Cross Section for the Raman Effect in Molecular Nitrogen Gas. *J. Opt. Soc. Am.* **1973**, *63*, 1604–1606.

51. Stockman, M. I.; Shalaev, V. M.; Moskovits, M.; Botet, R. Enhanced Raman Scattering by Fractal Clusters: Scale-Invariant Theory. *Phys. Rev. B* **1992**, *46*, 2821–2831.

52. Head-Gordon, M.; Tully, J. C. Electric Field Effects on Chemisorption and Vibrational Relaxation of CO on Cu-(100). *Chem. Phys.* **1993**, *175*, 37–51.

53. Wasileski, S. A.; Weaver, M. J.; Koper, M. T. M. Potential-Dependent Chemisorption of Carbon Monoxide on Platinum Electrodes: New Insight from Quantum-Chemical Calculations Combined with Vibrational Spectroscopy. *J. Electroanal. Chem.* **2001**, *500*, 344–355.

54. Kresse, G.; Gil, A.; Sautet, P. Significance of Single-Electron Energies for the Description of CO on Pt(111). *Phys. Rev. B* **2003**, *68*, 073401–073404.

55. Gajdo, M.; Eichler, A.; Hafner, J. CO Adsorption on Close-Packed Transition and Noble Metal Durfaces: Trends from *Ab Initio* Calculations. *J. Phys: Condens. Matter* **2004**, *16*, 1141–1164.

56. Persson, B. N. J.; Persson, M. Vibrational Lifetime for CO Adsorbed on Cu(100). *Solid State Commun.* **1980**, *36*, 175–179.

57. Tully, J. C.; Gomez, M.; Head-Gordon, M. Electronic and Phonon Mechanisms of Vibrational Relaxation: CO on Cu(100). *J. Vac. Sci. Technol., A* **1993**, *11*, 1914–1920.

58. Nanba, T.; Yamamoto, I.; Ikezawa, M. Surface Enhanced Raman Scattering of CO Adsorbed on Silver Film. *J. Phys. Soc. Jpn.* **1955**, *1986*, 2716.

59. Pettenkoffer, C.; Otto, A. "Chemical Effects" of Vibrational Lifetime and Frequency of CO on Ag. *Surf. Sci.* **1985**, *151*, 37–51.

60. Rydberg, R. Vibrational Line Shape of Chemisorbed CO. *Phys. Rev. B* **1985**, *32*, 2671–2673.

61. Ru, E. C. L.; Grand, J.; Fe, N.; Aubard, J.; Le, G.; Hohenau, A.; Krenn, J. R. Experimental Verification of the SERS Electromagnetic Model beyond the $|E|^4$ Approximation: Polarization Effects. *J. Phys. Chem. C* **2008**, *112*, 8117–8121.

62. Bosnick, K. A.; Jiang, J.; Brus, L. E. Fluctuations and Local Symmetry in Single-Molecule Rhodamine 6G Raman Scattering on Silver Nanocrystal Aggregates. *J. Phys. Chem. B* **2002**, *106*, 8096–8099.

63. Moore, A. A.; Jacobson, M. L.; Belabas, N.; Rowlen, K. L.; Jonas, D. M. 2D Correlation Analysis of the Continuum in Single Molecule Surface Enhanced Raman Spectroscopy. *J. Am. Chem. Soc.* **2005**, *127*, 7292–7293.

64. Lombardi, J. R.; Birke, R. L. Excitation Profiles and the Continuum in SERS: Identification of Fano Line Shapes. *J. Phys. Chem. C* **2010**, *114*, 7812–7815.

65. Otto, A.; Akemann, W.; Pucci, A. Normal Bands in Surface-Enhanced Raman Scattering (SERS) and Their Relation to the Electron–Hole Excitation Background in SER. *Isr. J. Chem.* **2006**, *46*, 307–315.

66. Michaels, A. M.; Nirmal, M.; Brus, L. E. Surface Enhanced Raman Spectroscopy of Individual Rhodamine 6G Molecules on Large Ag Nanocrystals. *J. Am. Chem. Soc.* **1999**, *121*, 9932–9939.

67. Galperin, M.; Ratner, M. A.; Nitzan, A. Raman Scattering from Nonequilibrium Molecular Conduction Junctions. *Nano Lett.* **2009**, *9*, 758–762.

68. Grover, S.; Moddel, G. Applicability of Metal/Insulator/Metal (MIM) Diodes to Solar Rectennas. *IEEE J. Photovoltaic* **2011**, *1*, 78–83.

69. Guarrotxena, N.; Ren, Y.; Mikhailovsky, A. Raman Response of Dithiolated Nanoparticle Linkers. *Langmuir* **2011**, *27*, 347–351.

70. Becke, A. D. Density-Functional Thermochemistry. III. The Role of Exact Exchange. *J. Chem. Phys.* **1993**, *98*, 5648–5652.

71. Schafer, A.; Huber, C.; Ahlrichs, R. Fully Optimized Contracted Gaussian-Basis Sets of Triple Zeta Valence Quality for Atoms Li to Kr. *J. Chem. Phys.* **1994**, *100*, 5829–5835.